Mechanisms of spin-charge conversion for the electrical readout of $4f$ quantum states in a $TbPc_2$ single-molecule magnet spin transistor

Kieran Hymas and Alessandro Soncini*
School of Chemistry, University of Melbourne, Parkville 3010, Australia

(Received 27 April 2020; revised 15 July 2020; accepted 16 July 2020; published 31 July 2020)

We present a theoretical study exposing the dominant microscopic electronic transport mechanisms underlying a recent molecular spin-transistor experiment [C. Godfrin *et al.*, ACS Nano **11**, 3984 (2017)], where purely electrical readout of the spin of a Tb(III)-based single-molecule magnet was achieved. To identify the relevant spin-to-charge conversion mechanisms enabling opposite spin polarizations of the Tb(III) ion $4f$ electrons to generate different magnetoconductance responses, we investigate both incoherent sequential tunneling charge transport, and coherent cotunneling corrections. Contrary to previous interpretations invoking the highly coherent Kondo transport regime, we find that all reported experimental observations, including the temperature and magnetic field dependence of the differential conductance, can be reproduced reasonably well within a sequential tunneling transport regime explicitly accounting for broadening of the device energy levels due to molecule-lead coupling.

DOI: 10.1103/PhysRevB.102.045313

I. INTRODUCTION

Single-molecule magnets (SMMs) have been proposed as candidates for molecular memory [1], molecular qubits [2,3], and for novel molecular spintronics applications [4,5] owing to their large magnetic anisotropy, stability upon surface and thin-film deposition, and their unique, rich, quantum properties. The *bis*-(phthalocyaninato) terbium nanomagnet ($TbPc_2$), in particular, has recently enjoyed a great deal of popularity in molecular spintronics setups, such as in molecular spin-valve experiments on graphene surfaces [6] and carbon nanotubes [7,8], when probed in thin films via scanning tunneling microscopy tips [9,10] and also in molecular break junctions [11–13].

The break-junction device has become a system of keen interest due to the potential of the weakly decohering ^{159}Tb nuclear states to act as a qudit computational basis for molecular quantum computation technologies [14,15]. The electrical readout of the ^{159}Tb nuclear spin computational basis is fundamentally rooted in a two-step coupling mechanism: (i) the ^{159}Tb nuclear spin is hyperfine coupled to the doubly degenerate $m_J = \pm 6$ $4f$-electron states of the Tb(III) ion, (ii) the $m_J = \pm 6$ states are, in turn, ferromagnetically exchange coupled to a radical $s = \frac{1}{2}$ spin hosted by the Pc_2 organic ligands of the nanomagnet, which are coupled to the Au-nanowire break junction, thus part of a sequential tunneling current in and out of the leads. The coupling between the sequential tunneling conduction electron hosted as a Pc_2 $s = \frac{1}{2}$ radical, and the $4f$ hyperfine states, enables the transfer of the nuclear spin states quantum information to the device current, resulting in a readout process [11,12,14].

Several experimental works reporting highly anisotropic hysteresis loops of conductance measurements recorded from the break junction [11] and from similar $TbPc_2$ setups [16,17] have demonstrated that the bistable electronic ground state of the $TbPc_2$ may be read out electronically by virtue of an exchange coupling between the Tb(III) electronic states and conduction electrons that transiently occupy the Pc ligands of the molecule.

Despite the many experimental results concerning this terbium molecular break-junction device, to our knowledge, fewer theoretical investigations have been undertaken to model electron transport through the system, and to understand the microscopic mechanism for the resultant readout of the Tb(III) electronic states. In a recent joint theoretical and experimental study of the device by Troiani *et al.* [18] the Landau-Zener-type tunneling dynamics of the Tb $4f$-electron states was investigated under continuous measurement from a local electric current, and simulated via a Lindblad-type master equation. The work focused in particular on identifying the signature of decoherence in the $4f$-electron tunneling dynamics, as measured by the transport experiments, using a phenomenological simulation of the coupling to the environment. However, the specific microscopic mechanisms of the transport measurement process, as those of the coupling to the environment, were not the object of that work.

In all previous experimental studies [11–13,18,19], the flipping of the terbium moment between the the $m_J = 6$ and -6 ground states was detected by measuring the differential conductance of the device as a function of an applied magnetic field, which was shown to give rise to disparate conductance signals for different initializations of the Tb $4f$ state. The transport measurements were always interpreted within a highly coherent and strongly correlated transport regime (Kondo transport), which entails the assumption of a strong coupling between the Au-nanowire junction and the Pc ligands of the $TbPc_2$ molecule.

The main evidence for a highly coherent transport regime, presented especially by Godfrin *et al.* [19], consisted of the

*asoncini@unimelb.edu.au

following points: (i) the conductance was probed at zero-bias voltage in gate-voltage detuned conditions, i.e., away from charge resonance points, which should suppress sequential tunneling via Coulomb blockade; (ii) the observed temperature dependence of the differential conductance displayed features that are reminiscent of Kondo transport through a simple $s = \frac{1}{2}$ quantum dot device, e.g., the conductance is maximal at the lowest temperatures, only to decay at higher temperatures.

We note that in Ref. [19], in order to model the observed magnetic field dependence of the differential conductance, it was necessary to assume that the anisotropic exchange coupling between the conduction electron and the Tb $4f$ electrons features a strong component perpendicular to the $TbPc_2$ easy axis (roughly 60% of the parallel component). However, such an assumption appears to be at variance with previous experimental [20] and *ab initio* [21–23] results on $4f$-Pc radical exchange coupling in $[TbPc_2]^0$, which instead all corroborate a more likely Ising purely axial anisotropic exchange mechanism, having negligible perpendicular component. Furthermore, the stability diagram reported by Godfrin *et al.* [19] appears to only weakly depart from a clear-cut Coulomb blockade diamond diagram, as the gate-detuned conductance appears to die off quite quickly as a function of gate voltage instead of clearly being established in the Coulomb blockaded dark regions. Finally, we also note that the assumption of strong molecule-lead coupling is not commonly observed in nanomagnet-based spintronics setups [6,24,25].

Prompted by these observations, in this paper we take a rather different interpretation of the transport experiments reported for the $TbPc_2$ spin-transistor device, and we present a theoretical model that primarily describes transport within the sequential tunneling regime, in the presence of broadening arising from the coupling to the leads. Using our model, we show that sequential tunneling indeed suffices to explain most features of the magnetoconductance reported in previous works [11,19], thus suggesting that electrical readout of a single spin can be achieved even without assuming a strong molecule-lead coupling, arguably easier to attain, hence more common, experimental outcome in device fabrication. Finally, we also explore coherent cotunneling corrections to the transport problem and discuss the significance and limitations of our model.

II. THEORETICAL MODEL

In the simplest approximation, the $TbPc_2$ nanomagnet molecular break junction consists of two electronic leads assumed here to be weakly hybridized with a readout quantum dot (the phthalocyaninato ligands of the nanomagnet), which in turn coordinate the central Tb(III) ion. Also, recent experimental works [11,12] have demonstrated a sizable hyperfine coupling between the $^{159}TbPc_2$ nucleus and its $|m_J = \pm 6\rangle$ $4f$-electronic states, however, we find that our results remain invariant to the inclusion of this coupling for the magnetic field strengths explored herein (see Appendix A) and so, for simplicity, we proceed by neglecting this coupling from our model. To model low-energy electron transport through the $TbPc_2$ device we partition the Hamiltonian as $H = H_L + H_S + H_T$, which describes the two noninteracting electronic leads H_L, the nanomagnet exchange coupled to the readout dot H_S, and the electron tunneling between each subsystem H_T, respectively. More specifically, the lead Hamiltonian reads as $H_L = \sum_{\alpha k\sigma} \epsilon_{\alpha k\sigma} a^\dagger_{\alpha k\sigma} a_{\alpha k\sigma}$ and describes the noninteracting electrons in lead $\alpha \in \{S, D\}$ with wave vector $\boldsymbol{k}$, spin σ, and energy $\epsilon_{\alpha k\sigma}$. The $a^{(\dagger)}_{\alpha k\sigma}$ hence form a set of annihilation (creation) operators that act on the single-particle states $|\alpha \boldsymbol{k}\sigma\rangle$ of each electrode. The hybridization between the readout dot and the leads is given by $H_T = \sum_{\alpha k\sigma} T^*_{\alpha k\sigma} a^\dagger_{\alpha k\sigma} d_\sigma + T_{\alpha k\sigma} d^\dagger_\sigma a_{\alpha k\sigma}$ where $d^{(\dagger)}_\sigma$ annihilates (creates) an electron with spin σ on the readout dot and $T_{\alpha k\sigma}$ represents an amplitude that quantifies the strength of the coupling between the readout dot and the leads. The low-energy spectrum of the terbium nanomagnet exchange coupled to a readout dot is modeled effectively by

$$H_S = \sum_\sigma (\epsilon_D - eV_g) d^\dagger_\sigma d_\sigma + \mu_B B(g_J J_z + g s_z) - a J_z s_z, \quad (1)$$

where ϵ_D is the energy of the lowest unoccupied molecular orbital (LUMO) of the phthalocyaninato ligands which constitute the readout dot and is modulated by some local gate voltage V_g, J_z and s_z are angular momentum operators that retrieve the projection of the total angular momentum in the ground-state spin-orbit multiplet of Tb(III) along the $TbPc_2$ magnetic anisotropy axis (z axis), and the spin projection along the same axis of the unpaired conduction electron hosted on the Pc_2 ligand readout dot, respectively, $\mu_B B$ is the amplitude of a longitudinally applied magnetic field premultiplied by the Bohr magneton, g_J is the Landé g factor for the ground $^7F_6$ spin-orbit multiplet of the Tb(III) ion, g is the g factor for a free electron, and, finally, a is the ferromagnetic coupling constant ($a > 0$) describing the Ising exchange coupling [20,23] between $4f$ electrons on the Tb(III) ion and unpaired electrons on the Pc_2 ligands (i.e., the readout dot).

For Eq. (1) to give a faithful representation of the low-energy spectrum of the $TbPc_2$ device, a few assumptions have been made that are well justified for this molecular device. First, we assume that the $TbPc_2$ magnet retains the large splitting (>400 cm^{-1}) between the ground and first excited crystal-field states within the lowest $^7F_6$ spin-orbit multiplet [21–23,26,27] when embedded in the break-junction device. This assumption is consistent with the fact that magnetic hysteresis measurements indicate the preservation of the nanomagnet's magnetic anisotropy axis [11]. Owing to the sub-Kelvin temperatures explored in these experiments, this assumption allows us to safely discard all but the two maximal total angular momentum projections $|m_J = \pm J\rangle$ from our model and consider the Tb(III) moment as a semiclassical Ising spin. Second, on the basis of experimental evidence [20] and high-level scalar relativistic multireference *ab initio* calculations [23], we describe the Tb(III) $4f$-electron-Pc_2 radical exchange coupling in terms of a purely axial Ising exchange-coupling Hamiltonian, which would result from projection of, e.g., an isotropic Heisenberg exchange Hamiltonian, onto the doubly degenerate thermally isolated ground state $|m_J = \pm 6\rangle$ of this molecule. This SMM radical exchange-coupling scheme then offers the simplest paradigm in which to capture theoretically the physics of the $TbPc_2$ molecular break junction. As a consequence of these assumptions, H_S is diagonal on the product basis of the nanomagnet's

bistable ground states and the spin states of the readout dot $|m;\sigma\rangle \equiv |m = \pm J\rangle_{\rm SMM} \otimes |\sigma\rangle$ which we will utilize for the rest of the paper.

A. Coulomb blockade transport model

We now discuss the theoretical framework in which we model the most relevant experimental quantity of the device: the zero-bias differential conductance. In order to study the relationship between the orientation of the Tb magnetic moment and conductance measurements at finite field, i.e., the very origin of the electrical readout mechanism observed in experiments [11,12,18,19], we compute contributions to the conductance from each orientation separately, and average the two signals when appropriate. The linear response differential conductance for one of the two possible orientations ($m = \pm 6$) of the semiclassical $TbPc_2$ Ising magnetic moment m is defined by the derivative of the steady-state current with respect to bias voltage

$$g_m = \left.\frac{dI_m}{dV_b}\right|_{V_b=0} = e\left.\frac{d}{dV_b}(\mathbf{W}_m \cdot \mathbf{P}_m)\right|_{V_b=0} = e\left.\left(\frac{d\mathbf{W}_m}{dV_b}\cdot \mathbf{P}_m + \mathbf{W}_m \cdot \frac{d\mathbf{P}_m}{dV_b}\right)\right|_{V_b=0}, \tag{2}$$

where $\mathbf{P}_m = (p_m, p_{m;\uparrow}, p_{m;\downarrow})^T$ contains the nonequilibrium populations of the electronic states of the device for a given orientation of the Tb moment m and $\mathbf{W}_m$ is a vector of transition rates between the redox states of the device obtained from the Fermi golden rule. As a result of weak but non-negligible coupling of the readout Pc_2 ligand-dot orbital state to the continuum of states in the leads, the molecular energy levels obtain a finite linewidth proportional to the imaginary part of the self-energy, arising as a correction to the effective molecular Hamiltonian to account for the coupling to the leads states, after eliminating the leads manifold from the full molecule-lead partitioned Hamiltonian [28]. The ensuing broadening of the molecular effective Hamiltonian eigenvalues (energy levels) is encoded in the spectral density function of the readout dot, which can be approximated as a Lorentzian line shape centered at the LUMO energy of the noninteracting Pc_2 ligand. We include this important effect into our model phenomenologically by expressing charge-transfer processes as convolutions of the leads' thermal functions with a Lorentzian line shape centered at the charging energy [29]

$$W_{\alpha\sigma}^{m\to m;\sigma'} = \frac{\Gamma\delta_{\sigma\sigma'}}{\hbar\pi}\int \frac{f(\epsilon-\mu_\alpha)\eta\, d\epsilon}{(\epsilon - \Delta_{m;\sigma',m})^2 + \eta^2}. \tag{3}$$

Here, $\Gamma = 2\pi\,\rho_{\alpha k\sigma}|T_{\alpha k\sigma}|^2$ is the coupling strength between the leads and the dot that, to a good approximation, can be taken as constant over the energy range explored herein [30,31], $\delta_{\sigma\sigma'}$ is a Kronecker delta function accounting for the overlap between the incoming electron spin and the reduced state, $\Delta_{m;\sigma',m}$ is the energy gap between the relevant reduced and uncharged states of the device, η is the hybridization-induced broadening of the molecular energy levels and $f(\epsilon-\mu_\alpha) = \{1+\exp[(\epsilon-\mu_\alpha)/k_BT]\}^{-1}$ is the Fermi-Dirac distribution of electrons in lead α at some temperature T and chemical potential $\mu_\alpha = \pm V_b$. The discharging rate of a spin σ electron to lead α is given by $W_{\alpha\sigma}^{m\sigma'\to m}$ and is readily obtained from Eq. (3) with the substitution $f(\epsilon-\mu_\alpha) \to [1 - f(\epsilon-\mu_\alpha)]$.

In order to evaluate the conductance formula in Eq. (2) we compute the populations of the electronic states of the device from a quantum rate equation that describes the nonequilibrium dynamics imparted on the molecular system as a result of coupling to the leads [32]. The time evolution of each population is determined by

$$\begin{aligned}\dot{p}_m &= \sum_\sigma W^{m;\sigma\to m} p_{m;\sigma} - p_m W^{m\to m;\sigma},\\ \dot{p}_{m;\sigma} &= W^{m\to m;\sigma} p_m - p_{m;\sigma} W^{m;\sigma\to m},\end{aligned} \tag{4}$$

where the charging rates summed over leads and spin are $W^{m\to m;\sigma} = \sum_{\alpha\sigma'} W_{\alpha\sigma'}^{m\to m;\sigma}$ and likewise for the discharging rates. As we are interested only in the steady-state limit of Eq. (4) we solve the linear system that originates when $\dot{\mathbf{P}}_m = 0$ with the additional normalization condition $p_m + p_{m;\uparrow} + p_{m;\downarrow} = 1$.

A final simplification to our model can be made by noting that if our device is invariant under a parity transformation, which in our simple model is tantamount of assuming that the molecular device is symmetrically coupled to left and right leads, then the nonequilibrium populations of the single-level quantum dot are invariant under reversal of the bias voltage. On the other hand, the bias-voltage drop across the device is by definition odd under a parity transformation. Hence, the Taylor series expansion about $V_b = 0$ of the populations in powers of the external bias voltage must necessarily be an even polynomial in the bias voltage, so that all odd derivatives of the populations with respect to the bias evaluated at zero bias must be identically zero. In particular, we have $d\mathbf{P}_m/dV_b = 0$ at zero bias, which simplifies Eq. (2), leading to the compact formula

$$g_m|_{V_b=0} = e\left.\left(\frac{d\mathbf{W}_m}{dV_b}\cdot\mathbf{P}_m\right)\right|_{V_b=0} \tag{5}$$

for the zero-bias differential conductance. An alternative proof of Eq. (5) is presented in Appendix B. We note that the fabrication of a molecular device with a perfectly symmetrical source/drain coupling (i.e., $\Gamma_S = \Gamma_D = \Gamma$) is somewhat unlikely, hence limiting the scope of Eq. (5) for realistic devices. However, introducing such a lead-dot coupling asymmetry does not change the essential physics exposed by our model (see Appendix A) and so we proceed with this none-too-restrictive assumption for simplicity.

We now discuss in some detail sequential tunneling transport occurring via two different exchange-coupling regimes in which, through different mechanisms, it is possible to explain the observed electric readout of the quantum states of the $TbPc_2$ nanomagnet embedded in the molecular break-junction device.

1. Large exchange-coupling regime: Gate-detuning-driven readout mechanism

We begin with a study of the coupling between the Tb $4f$ electrons and the unpaired conduction electron hosted on the Pc_2 dot in the large ferromagnetic exchange regime [$6a \gg k_BT$, where $6a$ is the exchange energy gap according

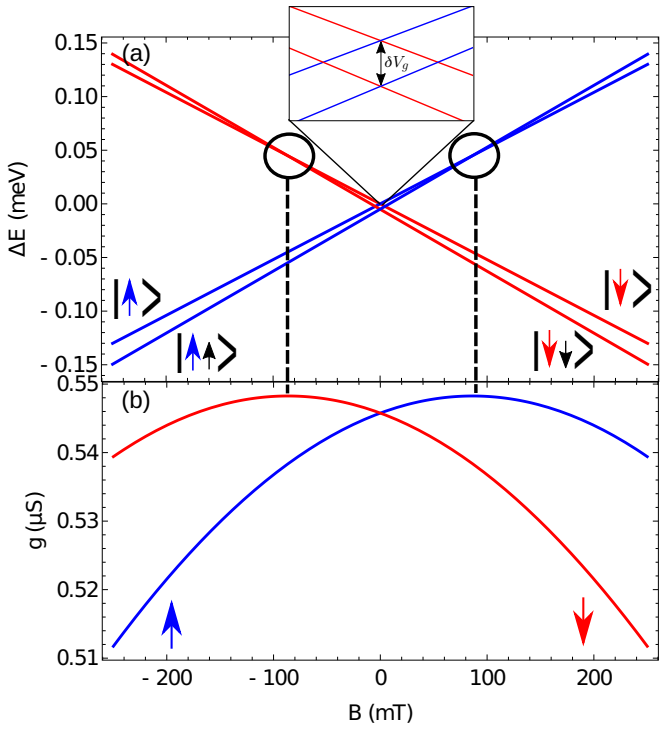

FIG. 1. (a) Zeeman diagram of the lowest-lying levels of the device in the large exchange-coupling regime. (b) Conductance as a function of magnetic field at 100 mK for the two orientations of the $TbPc_2$ magnetic moments $m = J$ (spin up, blue arrow) and $m = -J$ (spin down, red arrow) in the large exchange-coupling regime. Note the conductance peaks at the magnetic field values $B = \pm 2\delta V_g/g\mu_B$, at which values the gate-voltage-detuned energies of the neutral and reduced states of the $TbPc_2$ are brought back to charge resonance.

to Eq. (1)], so that the antiferromagnetically coupled reduced states $|m = \pm J, \sigma = \mp\frac{1}{2}\rangle$ are thermally isolated and do not participate in electron transport. We choose a gate voltage $V_g = V_g^{(0)} + \delta V_g$, where $V_g^{(0)}$ is the gate that brings to degeneracy at zero field the ferromagnetic reduced state $|m = \pm J, \sigma = \pm\frac{1}{2}\rangle$ and the uncharged state $|m = \pm J\rangle$. As shown in the Zeeman energies plot in Fig. 1(a), the effect of δV_g is to shift the system away from charge resonance (gate detuning), preparing the system in a ferromagnetic reduced ground state. Note that, in our model, the role of detuning is to shift the charge resonance degeneracies between the uncharged and reduced ground states, hence, the peaks of the sequential tunneling current, to nonzero values of the magnetic field, having opposite signs for opposite orientations of the Tb magnetic moment [circled in black in Fig. 1(a)].

For a given orientation of the terbium magnetic moment m the conductance [obtained from Eq. (5)] takes on the particularly simple form

$$g_m|_{V_b=0} = \frac{e\Gamma}{2\pi\hbar}\int \frac{\eta\, d\epsilon}{(\epsilon + \delta V_g - g\mu_B B\sigma)^2 + \eta^2} \times \left(\frac{\partial f(\epsilon - V_b)}{dV_b} - \frac{\partial f(\epsilon + V_b)}{dV_b}\right)\Big|_{V_b=0}. \quad (6)$$

It is instructive to take the zero-temperature limit of Eq. (6), so that the Fermi-Dirac functions become step functions whose derivatives are Dirac delta functions centered at $V_b = 0$. In this limit the integral in Eq. (6) can be evaluated exactly, and it can be readily seen that the zero-temperature limit of the conductance for each orientation of the $TbPc_2$ moment as a function of the magnetic field is proportional to a Lorentzian line shape peaked at $B = \pm 2\delta V_g/g\mu_B$, where the $\pm$ corresponds to the $m = \pm J$ orientation of the Tb magnetic moment. From this analysis we can ascribe the splitting of the conductance signals in an applied magnetic field for each transport channel $m = \pm J$ at zero bias and low temperature to an off-resonance phenomenon that originates from detuning the electronic levels of the Tb-dot hybrid away from level degeneracy with a gate voltage, then restored by a magnetic field together with the peaks of maximal differential conductance.

With the above mechanism in mind, we calculate the conductance as a function of magnetic field for both orientations of the $TbPc_2$ moment at the finite temperature $T = 100$ mK used in the experiment [19] by numerical integration of Eq. (6). We obtain best agreement with the experiments for molecule-leads tunnel coupling $\Gamma/\hbar = 6.5\times10^8$ s^{-1}, and using a broadening factor $\eta = 55$ μeV, which is of the order of magnitude of the broadening used to model electron transport through quantum dots [29,33]. Furthermore, in order to reproduce the conductance peaks at the experimentally observed fields of $B = \pm 100$ mT, within the strong coupling regime the detuning gate voltage must be fixed at $\delta V_g \approx 0.005$ meV. Figure 1(b) shows the calculated conductance as a function of magnetic field for each orientation of the Tb magnetic moment. The peaks in the conductance associated to each orientation of the Tb moment clearly originate from a recovery of the level degeneracy condition restored via the magnetic field. In this regime, applying a static magnetic field to the device leads to two disparate conductance signals that provide an electronic readout of the spin state of the terbium nanomagnet, explaining the observed readout experiments [18,19] within the Coulomb blockade transport regime.

We note that recent multifrequency electron paramagnetic resonance (EPR) experiments on single crystals of this spin-transistor molecular unit $[TbPc_2]^0$ measured an intramolecular $4f$-electron-Pc_2 radical Ising exchange energy gap of $6a = 0.11$ meV ($a \approx 0.02$ meV) [20]. Given that the thermal energy available at $T = 100$ mK ($\approx$0.01 meV) is 10 times smaller than the experimental exchange gap, we would expect the strong exchange limit discussed in this section to be the relevant exchange-coupling regime to describe the readout mechanism observed for this molecular spin transistor. This could be easily verified within the spin-transistor experimental setup by monitoring as function of applied gate voltage the magnetic field values for which the conductance peaks are observed. We have not so far been able to find these data in the literature.

2. Weak exchange-coupling regime: Exchange-driven readout mechanism

We now proceed with a discussion of the weak exchange-coupling regime ($6a \lesssim k_B T$), where both the ferromagnetic and antiferromagnetic reduced states participate in electronic transport through the device. We set the exchange-coupling constant to $a = 2\times10^{-3}$ meV, which is one order of

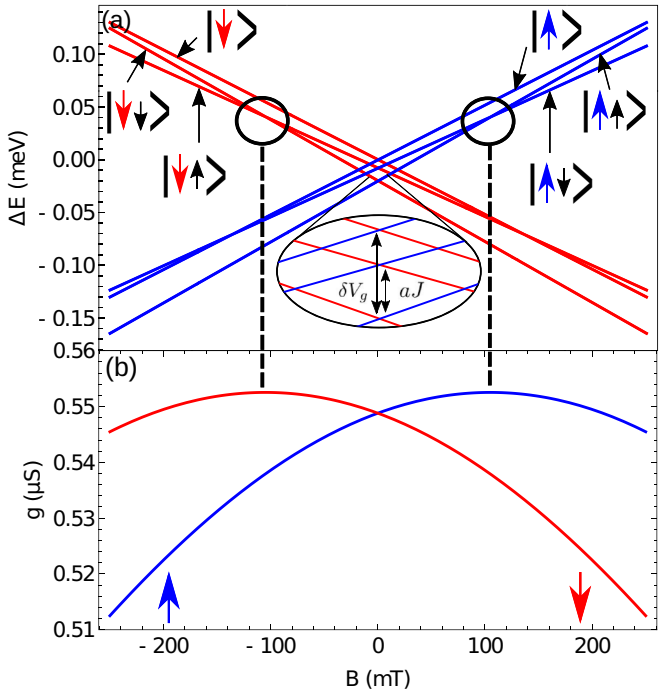

FIG. 2. (a) Zeeman diagram of the lowest-lying levels of the device in the weak exchange-coupling regime where $a < \delta V_g$. (b) Conductance as a function of magnetic field at 100 mK for the two orientations of the $TbPc_2$ magnetic moments $m = J$ (spin up, blue arrow) and $m = -J$ (spin down, red arrow) in the weak exchange-coupling regime. Note that in this case, the conductance peaks at the magnetic field values $B = \pm aJ/g\mu_B$, at which values the exchange-coupling split energies of the ferromagnetic and antiferromagnetic reduced states of $TbPc_2$ become degenerate.

magnitude smaller than that measured in single-crystal experiments [20], hence comparable to the thermal energy available at $T = 100$ mK. The ensuing Zeeman spectrum of the device, assuming a detuning gate voltage $\delta V_g = 0.02$ meV, is reported in Fig. 2(a).

In order to simulate the finite-temperature sequential tunneling transport, we use Eq. (5) as function of the external magnetic field, and plot the differential conductance as function of field in Fig. 2(b). The best agreement with experiments was obtained for $\Gamma/\hbar = 6.7\times10^8$ s^{-1} and $\eta = 75$ μeV.

As shown in Fig. 2(b), also in the weak exchange-coupling regime the two opposite spin polarizations of the Tb(III) nanomagnet give rise to well-defined disparate conductance signals at finite applied field, peaked at the same but opposite nonzero values of the external magnetic field, reproducing the experimental observations (peaks are centered at $B = 100$ mT). However, inspection of the Zeeman energy diagram reported in Fig. 2(a) immediately shows that the peaks of conductance in this case coincide with field-induced level crossings *within the same redox manifold*, i.e., at $B =$ 100 mT we recover degeneracy between the ferromagnetic and antiferromagnetic reduced states only, as opposed to the large exchange-coupling regime reported in Fig. 1, where the peaks correspond to charge resonance points at level degeneracies between different charged and uncharged redox states. The reason why the conductance peaks at the level

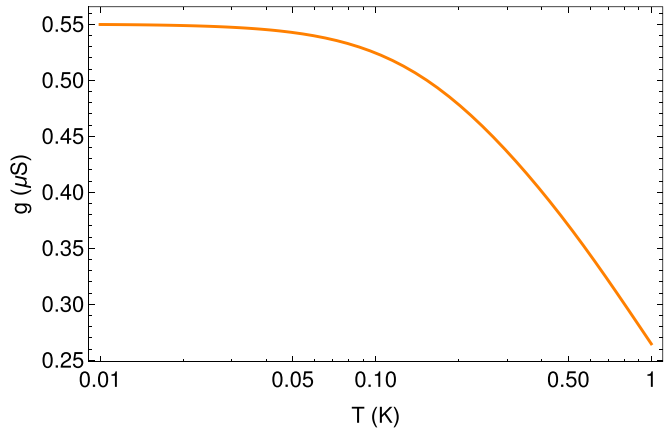

FIG. 3. Differential conductance averaged over both orientations of the Tb moment as a function of temperature using $a = 0.02$ meV. Best agreement with experiments was obtained for $\Gamma/\hbar = 6.6\times10^8$ s^{-1}, and $\eta = 65$ μeV.

crossing between same-redox states, occurring at field values $B = \pm aJ/g\mu_B$ [circled in black in Fig. 2(b)], is that at these crossings the steady-state populations of the reduced states become equal, and hence contribute simultaneously and maximally to transport through the device.

As the amplitude of the magnetic field required to bring the reduced states to degeneracy is unaffected by gate detuning, the positions of the differential conductance signals in this regime are sensitive only to the value of the exchange gap $6a$, hence implementing an exchange-driven readout mechanism, which is expected to be less sensitive to the detailed value of the detuning gate voltage used in the experiment. In this limit, the transport experiments would then provide a direct measure of the exchange-coupling strength between $4f$ electrons and the sequential tunneling electrons.

B. Temperature, magnetic field, and bias-voltage dependence of the conductance

To study the temperature, bias voltage, and magnetic field dependence of the device differential conductance we simulate sequential tunneling transport using the exchange coupling a observed in single-crystal EPR experiment [20] and corroborated by multiconfigurational [21–23] and multireference *ab initio* calculations [23], corresponding to $a \approx$ 0.02 meV, and leading to an exchange energy gap ≈0.1 meV, 10 times smaller than the thermal energy available at the operating temperature. While for this choice of coupling both of the aforementioned mechanisms could in principle play a role, we expect the gate-detuning-driven mechanism discussed for the limit $6a \gg k_BT$ to dominate, with only a negligible amount of population transfer to the antiferromagnetic reduced states of the device when the field is applied. We find that the effect of such population transfer is to shift the center of the peaks of differential conductance shown in Fig. 1(b) by a few tens of mT to higher fields.

In Fig. 3 the differential conductance in the absence of a magnetic field is plotted as a function of temperature. A plateau is observed in the conductance at low temperatures until $k_BT \sim \delta V_g$ wherein the electronic states of the device

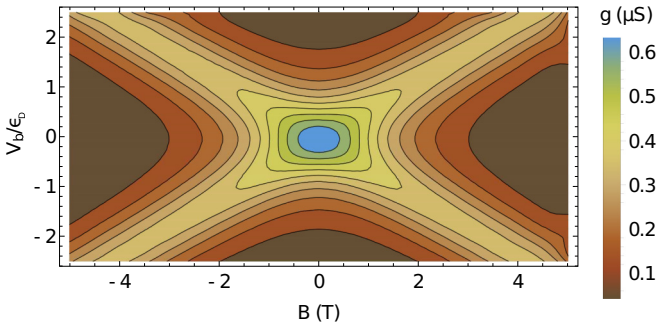

FIG. 4. Contour plot of conductance averaged over both orientations of the Tb moment as a function of bias voltage (in units of the occupation energy of the dot) and magnetic field, for $a = 0.02$ meV, $\Gamma/\hbar = 6.6\times10^{8}$ s^{-1}, and $\eta = 65$ μeV.

thermally equilibrate and the conductance signal begins to fall off to zero. We note that the behavior of the differential conductance as a function of temperature in our model captures the temperature dependence of the molecular break-junction device as reported in Ref. [19], except that in our microscopic model of sequential tunneling conductance we do not need to invoke Kondo coherent transport in order to reproduce this behavior. This specific line shape, then, appears to be a necessary but evidently not sufficient condition to infer the strongly correlated Kondo transport regime in this molecular device.

In Fig. 4 we report the differential conductance as a function of magnetic field and bias voltage. The strong, broad resonance about $B = 0$ and $V_b = 0$ can be attributed to the averaged conductance signals that appear for each orientation of the Tb moment [see Fig. 1(b)]. At zero-bias voltage and larger values of the magnetic field the level degeneracies between the uncharged states and the reduced states of the device are lost and the conductance signal falls to zero. For magnetic fields greater than the exchange coupling, the ferromagnetic reduced state becomes the ground state of the device which may transfer excess charge to electrodes and thus reinstate a sequential tunneling electric current through the device only when the bias conduction window is wide enough so as to include the uncharged ground state of the $TbPc_2$ molecule.

C. Coherent corrections to transport

To investigate the extent of the coherent character of the conductance in the $TbPc_2$ break junction, we consider corrections to the Coulomb blockade models presented above to second nonvanishing order (cotunneling) in the hybridization Hamiltonian H_T. To calculate the cotunneling rates we employ a T-matrix approach which is known to be consistent with a full microscopic derivation of the transport problem [34–36]. In this approach, there are three types of cotunneling processes that may contribute to the conductance within our model and for the experimental choice of gate-voltage detuning: (i) elastic transitions in the uncharged manifold, (ii) elastic transitions in the reduced manifold and (iii) inelastic transitions in the reduced manifold. The most general expressions for the cotunneling rates in the neutral and reduced manifolds, respectively, are [37]

$$W^{N,i\to f}_{a\sigma;a'\sigma'} = \frac{\Gamma^2}{2\pi\hbar}\int d\epsilon\, f_\alpha(\epsilon)[1-f_{\alpha'}(\epsilon-\Delta_{fi})] \times\left|\sum_\nu \frac{\langle f|d_\sigma|\nu\rangle\langle\nu|d^\dagger_{\sigma'}|i\rangle}{\epsilon-\Delta_{\nu i}+i\gamma}\right|^2,$$
$$W^{N+1,i\to f}_{a\sigma;a'\sigma'} = \frac{\Gamma^2}{2\pi\hbar}\int d\epsilon\, f_\alpha(\epsilon)[1-f_{\alpha'}(\epsilon-\Delta_{fi})] \times\left|\sum_\nu \frac{\langle f|d^\dagger_\sigma|\nu\rangle\langle\nu|d_{\sigma'}|i\rangle}{-\epsilon+\Delta_{f\nu}+i\gamma}\right|^2, \quad (7)$$

where the sums run over all virtual states $|\nu\rangle$ of the device that differ in electron number from the final and initial states $|f\rangle$ and $|i\rangle$ by 1. The finite lifetime γ for the virtually populated state has been included to regularize the denominators and, to a first approximation, the broadening of the molecular energy levels induced by the coupling to the leads is absorbed into the finite lifetime of the virtual transition so that $\gamma = \eta$. The quantum rate equations given in Eq. (4) for the reduced states must now be amended to account for population transfer as a result of inelastic cotunneling transitions (elastic cotunneling transition by definition do not change the populations of the states). The new rate equations for the reduced states are given by

$$\dot p_{m;\sigma} = W^{m\to m;\sigma}p_m + W^{N+1,m;\bar\sigma\to m;\sigma}_{\rm cot}p_{m;\bar\sigma} - p_{m;\sigma}\left(W^{m;\sigma\to m} + W^{N+1,m;\sigma\to m;\bar\sigma}_{\rm cot}\right), \quad (8)$$

where $|m;\bar\sigma\rangle$ denotes the reduced state other than $|m;\sigma\rangle$ and $W^{N+1,m;\sigma\to m;\bar\sigma}_{\rm cot} = \sum_{\alpha'\alpha''\sigma'\sigma''} W^{N+1,m;\sigma\to m;\bar\sigma}_{\alpha'\sigma';\alpha''\sigma''}$ are all possible inelastic cotunneling processes that transfer population from the state $|m;\sigma\rangle$ to $|m;\bar\sigma\rangle$. Likewise, the expression for the conductance is now recast to include all cotunneling contributions to electronic transport through the device. Again, using the parity invariance arguments outlined above, one obtains the compact formula

$$g_m|_{V_b=0} = e\left(\frac{d\mathbf{W}^{\rm seq}_m}{dV_b}+\frac{d\mathbf{W}^{\rm cot}_m}{dV_b}\right)\cdot\mathbf{P}_m\Big|_{V_b=0} \quad (9)$$

for the zero-bias steady-state conductance of the device where the appropriate transition rates for sequential tunneling and cotunneling have been collected into the vectors $\mathbf{W}^{\rm seq}_m$ and $\mathbf{W}^{\rm cot}_m$, respectively.

1. *Large exchange-coupling regime*

We consider again the large exchange-coupling regime in which the antiferromagnetic reduced states of the device are thermally inaccessible for transport. As a consequence of this large coupling, all inelastic cotunneling transitions between the ferromagnetic and antiferromagnetic reduced states are suppressed and the steady-state quantum rate equations for all states in the device remain identical to the purely incoherent regime.

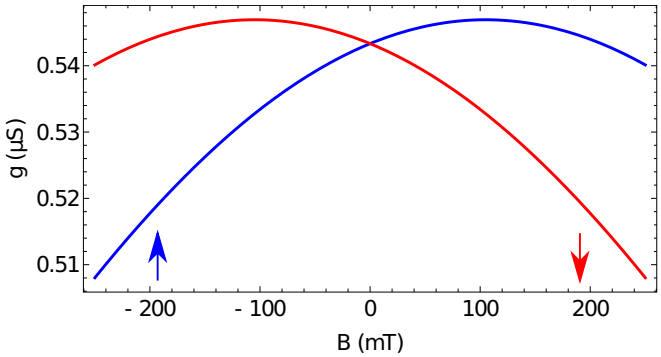

FIG. 5. Conductance as a function of magnetic field arising from sequential and cotunneling processes at $T = 100$ mK for the two orientations of the $TbPc_2$ magnetic moments $m = J$ (spin up, blue arrow) and $m = -J$ (spin down, red arrow) in the weak exchange-coupling regime.

The sequential tunneling contribution to the zero-bias steady-state conductance is

$$\frac{d\mathbf{W}_m^{\rm seq}}{dV_b}\cdot\mathbf{P}_m\bigg|_{V_b=0} = \frac{e\Gamma}{\pi\hbar k_B T}\int\frac{e^{\beta\epsilon}d\epsilon}{(1+e^{\beta\epsilon})^2} \times\frac{\eta}{(\epsilon-\Delta_{m;\sigma,m})^2+\eta^2} \tag{10}$$

while the elastic cotunneling contribution is

$$\frac{d\mathbf{W}_m^{\rm cot}}{dV_b}\cdot\mathbf{P}_m\bigg|_{V_b=0} = \frac{e\Gamma^2}{2\pi^2\eta\hbar k_B T}\int\frac{e^{\beta\epsilon}d\epsilon}{(1+e^{\beta\epsilon})^2} \times\frac{\eta}{(\epsilon-\Delta_{m;\sigma,m})^2+\eta^2}, \tag{11}$$

where $\beta = 1/k_B T$ and $\Delta_{m;\sigma,m}$ is the energy gap between the ferromagnetic reduced state and the neutral state of the device with Tb orientation m. Combining Eqs. (10) and (11) results in a formula for the conductance that is identical to the pure Coulomb blockade transport model described above, however, now with a renormalized coupling constant $\Gamma \mapsto \Gamma(1+\Gamma/2\pi\eta)$ between the dot and the leads. As before, even after including cotunneling processes into the model, the disparate signals of conductance that can be attributed to the individual quantum states of the nanomagnet result from an off-resonance effect induced by detuning the system from level degeneracy with a gate voltage.

2. Weak exchange-coupling regime

We briefly return to the weak exchange-coupling regime but now with the cotunneling corrections that were discussed above, included into the model. Using the same parameter set as discussed in the previous weak coupling section we simulated the differential conductance as a function of magnetic field for each orientation of the terbium magnetic moment as shown in Fig. 5. With coherent corrections included to second nonvanishing order of the perturbation theory, we observed no change to either the conductance in a magnetic field or to the temperature-dependent conductance as the cotunneling transition rates appeared two orders of magnitude smaller than the sequential charging and discharging rates.

III. CONCLUSIONS

In this work we presented two sequential tunneling theoretical models, which were shown to capture recent low-temperature experimental observations of off-charge resonance differential conductance as function of magnetic field, temperature, and bias voltage. The two separate mechanisms we have identified for the electric readout of the magnetic quantum state of the $TbPc_2$ in differential conductance measurements at finite magnetic field depend on the system's parameters in a fundamentally different way, which provides an experimental handle to check the prevalence of each regime in a given device.

Specifically, the peaks of the differential conductance readouts as function of magnetic field, for the two opposite orientations of the magnet in the large exchange-coupling regime, are found to be linearly dependent on the magnitude of the gate voltage shift from the $N/N+1$ charge resonance point. Conversely, the position of the same peaks of magnetoconductance in the weak exchange-coupling limit are mainly an expression of the Ising exchange-coupling strength between the Tb(III) nanomagnet $4f$ electrons and the sequential tunneling electron spin hosted by the molecule's Pc_2 ligand, and are not expected to change significantly on scanning a gate voltage across the charge resonance.

On the basis of the experimental value of the exchange-coupling energy gap ($6a \approx 0.1$ meV) for the $[TbPc_2]^0$ molecule in the crystal phase, assuming it is not significantly affected by coupling to the break-junction device or by the application of gate voltages, we argue that the gate-detuning-driven readout mechanism identified here in the large exchange-coupling regime is expected to be the most prominent for explaining the origin of the disparate signals of differential conductance measured for each of the $4f$ quantum ground states of the $TbPc_2$ nanomagnet.

On the basis of the good performance of our sequential tunneling model, including its simulation of the temperature dependence of the differential conductance line shape which was argued to be associated to a Kondo transport regime, we have provided evidence that the disparate conductance signals measured for each Tb magnetic moment orientation in a longitudinal magnetic field can be explained solely on the basis of sequential tunneling processes in the Coulomb blockade transport regime, with no essential need to invoke coherent transport regimes, as also shown by the negligible influence of the coherent cotunneling corrections explored here.

As such, while we cannot exclude that higher-order coherent conduction mechanisms might improve quantitative agreement between theory and experiment, we posit here that incoherent charge tunneling processes and the associated Coulomb blockade physics contributes dominantly to the low-temperature conductance of this device, which may contribute to explaining the microscopic mechanisms of dephasing in the Landau-Zener–type $4f$ spin-tunneling dynamics identified in recent studies of the $TbPc_2$ break junction [18]. This has significant implications for future studies of molecular spin transistors based on single-molecule magnets, as weak molecule-lead coupling represents a more common scenario in the fabrication of these devices, where selective control of the interactions between molecule and leads cannot as yet be easily achieved.

ACKNOWLEDGMENTS

K.H. acknowledges support from the Australian Government Research Training Program Scholarship. A.S. acknowledges support from the Australian Research Council (Future Fellowship No. FT180100519).

APPENDIX A: GENERAL MODEL: HYPERFINE COUPLING AND ASYMMETRIC COUPLING TO THE LEADS

In this Appendix we show that the relaxation of some of the constraints in our model (namely, the neglect of ^{159}Tb hyperfine coupling, and the symmetric coupling to the source and drain leads) does not change any of the conclusions achieved with the simpler and more symmetric model.

1. Hyperfine levels

To include the hyperfine structure of the ^{159}Tb nanomagnet into our model we append to Eq. (1) the Hamiltonian $H_{\rm nuc} = \mu_B B g_I I_z + A I_z J_z + P[I_z^2 + I(I+1)/3]$ which accounts in the first term for the Zeeman interaction of the ^{159}Tb nucleus, in the second term for the hyperfine interaction between the nucleus and the electronic angular momentum of the nanomagnet, and in the third term for the nonspherical, quadrupolar structure of the nucleus. Here, $g_I = 1.34$ is the nuclear g factor for terbium, $A = 2.14$ μeV is the hyperfine coupling constant, and $P = 1.24$ μeV as reported by Ishikawa *et al.* [38]. The new Hamiltonian $H_S' = H_S + H_{\rm nuc}$ is diagonal on the product basis of the nanomagnet's bistable ground states, nuclear spin states, and the spin states of the readout dot $|m, m_I, \sigma\rangle = |m = \pm J\rangle \otimes |m_I\rangle \otimes |\sigma\rangle$ where m_I can take on the values $\frac{-3}{2}$, $\frac{-1}{2}$, $\frac{1}{2}$, and $\frac{3}{2}$. The energies of these states are plotted as functions of magnetic field in the upper panel of Fig. 6(a) after detuning the system from level degeneracy with a gate voltage $\delta V_g = 0.005$ meV. Note that as a result of this detuning, the level degeneracies between the neutral and charged states with matching electronic and nuclear angular momentum quantum numbers are shifted [black circles in Figure 6(a)] to $B = \pm 2\delta V_g / g\mu_B$ *irrespective of the nuclear spin quantum number of the states*; note that the $\pm$ sign relates to the orientation of the $TbPc_2$ magnetic moment $m = \pm J$.

We proceed from here as in the main text by developing master equations for the populations of each orientation of the $TbPc_2$ magnetic moment and solve for the steady-state populations which are then used to compute the conductance from Eq. (5). In Fig. 6(b) we plot the resultant curves of magnetoconductance that arise for each orientation of the $TbPc_2$ moment utilizing the parameter set used to produce Fig. 1 in the main text. The invariance of our model upon the introduction of hyperfine coupling results from the inability of neutral and charged states with $m_I \neq m_I'$ to participate in charging/discharging events, thus, the only level degeneracies left that may contribute to the device conductance are unaffected by interactions with the ^{159}Tb nucleus. A similar argument can be made for the weak exchange-coupling regime wherein the magnetoconductance curves for each orientation of the $TbPc_2$ magnetic moment again remain invariant upon the inclusion of the hyperfine states of the device.

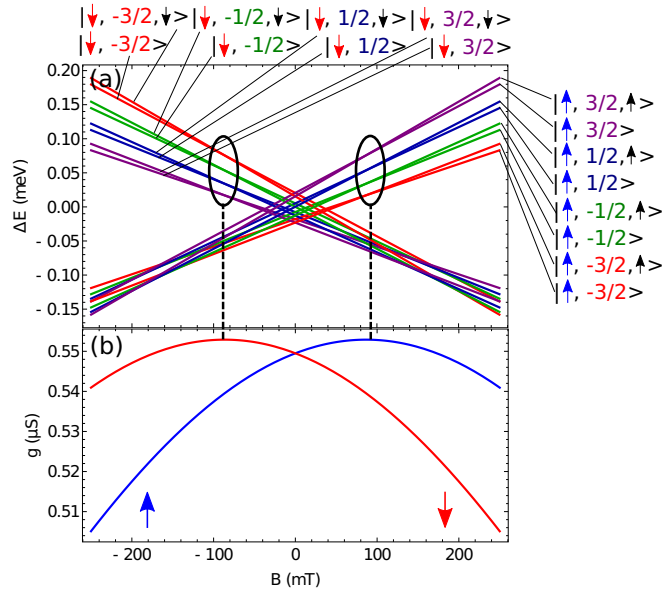

FIG. 6. (a) Zeeman diagram of the lowest-lying hyperfine-split levels of the device $|m, m_I, \sigma\rangle$ in the large exchange-coupling regime. (b) Conductance as a function of magnetic field at 100 mK for the two orientations of the $TbPc_2$ magnetic moments $m = J$ (spin up, blue arrow) and $m = -J$ (spin down, red arrow).

2. Asymmetric coupling

If the lead-dot coupling to source and drain is allowed to be different, we note that our simple expression for the conductance [given in Eq. (5)] is no longer valid. To ascertain the consequences of introducing such an asymmetry we implemented the full calculation of the conductance accounting for the derivative of the populations with respect to bias voltage [Eq. (2)] and report the results of the magnetoconductance for one orientation of the $TbPc_2$ magnetic moment as a function of magnetic field in Fig. 7. Notably, by varying the ratio between the lead-dot coupling constants for the source and drain, the magnetoconductance becomes diminished in magnitude but still retains its broad, Lorentzian line shape centered at $B = 2\delta V_g / g\mu_B$. Therefore, the appearance of a small asymmetry in the coupling constants Γ_S and Γ_D does not affect the readout mechanisms discussed in the main text

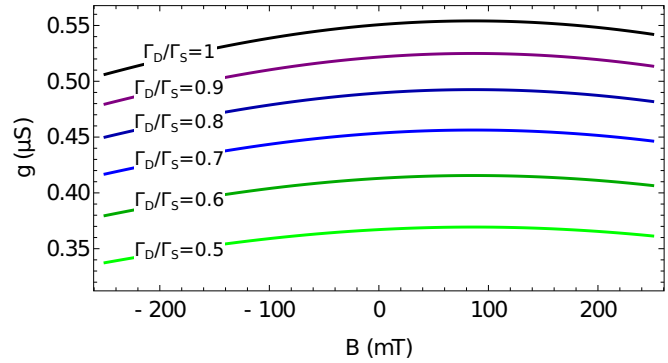

FIG. 7. Magnetoconductance of the device when $m = J$ in the large exchange-coupling regime at various ratios of lead-dot coupling Γ_D/Γ_S using the same parameter set as for Fig. 1 with $\Gamma_S = \Gamma$.

and can be accounted for in our more symmetric model by adjusting the value of Γ.

APPENDIX B: CONDUCTANCE FORMULA AT ZERO BIAS

We will now prove the validity of Eq. (5) from Eq. (2) which amounts to showing that the term proportional to $d\mathbf{P}_m/dV_b$ on the right-hand side of Eq. (2) vanishes when $V_b = 0$. The population vector $\mathbf{P}_m$ is obtained by solving the rate equations presented in Eq. (4). For ease of notation, we cast these equations into a matrix form and consider a derivative with respect to bias voltage V_b:

$$\frac{d\mathbf{P}_m}{dt} = \mathcal{M}\mathbf{P}_m \Rightarrow \frac{\partial}{\partial V_b}\frac{d\mathbf{P}_m}{dt} = \frac{\partial}{\partial V_b}(\mathcal{M}\mathbf{P}_m)$$
$$\Rightarrow \frac{d}{dt}\left(\frac{\partial \mathbf{P}_m}{\partial V_b}\right) = \mathcal{M}\frac{\partial \mathbf{P}_m}{\partial V_b} + \frac{\partial \mathcal{M}}{\partial V_b}\mathbf{P}_m. \quad \text{(B1)}$$

At zero-bias voltage, the last term on the right-hand side of Eq. (B1) is exactly zero. To see why this is the case, consider the derivative with respect to bias voltage of a representative coefficient of the matrix $\mathcal{M}$:

$$\frac{\partial W^{m\to m;\sigma'}}{\partial V_b} = \sum_{\alpha\sigma}\frac{\partial W^{m\to m;\sigma'}_{\alpha\sigma}}{\partial V_b}$$
$$= \int d\mu(\epsilon)\left[\frac{\partial f(\epsilon + V_b)}{\partial V_b} + \frac{\partial f(\epsilon - V_b)}{\partial V_b}\right], \quad \text{(B2)}$$

where $d\mu(\epsilon) = d\epsilon(\Gamma/\hbar\pi)[\eta/(\epsilon - \Delta_{m\sigma';m})^2 + \eta^2]$. Notably, in this step we have assumed a symmetric coupling strength between the dot and both leads, i.e., $\Gamma_S = \Gamma_D = \Gamma$. Clearly, when $V_b = 0$ the integrand vanishes due to the derivatives of the Fermi functions. The same calculation can be made for entries of $\mathcal{M}$ containing discharging rates, thus reducing Eq. (B1) to

$$\frac{d}{dt}\left(\frac{\partial \mathbf{P}_m}{\partial V_b}\right) = \mathcal{M}\frac{\partial \mathbf{P}_m}{\partial V_b} \quad \text{(B3)}$$

when $V_b = 0$. Equation (B3) has the exact form of the master equation for the populations $\mathbf{P}_m$ and thus possesses a steady-state limit, i.e., the matrix $\mathcal{M}$ has one zero eigenvalue. Second, note that $\sum_i \partial \mathbf{P}^i_m/\partial V_b = \partial/\partial V_b \sum_i \mathbf{P}^i_m = \partial/\partial V_b(1) = 0$, where we have used that the populations sum to unity. It can be readily verified then that the steady-state limit of $\partial \mathbf{P}_m/\partial V_b$ that is obtained from solving the linear system

$$\mathcal{M}\frac{\partial \mathbf{P}_m}{\partial V_b} = \mathbf{0} \quad \text{(B4)}$$

with the additional condition $\sum_i \partial \mathbf{P}^i_m/\partial V_b = 0$ is $\partial \mathbf{P}_m/\partial V_b = \mathbf{0}$ and, thus, at zero-bias voltage, Eq. (5) is retrieved.

[1] M. Mannini, F. Pineider, P. Sainctavit, C. Danieli, E. Otero, C. Sciancalepore, A. M. Talarico, M.-A. Arrio, A. Cornia, D. Gatteschi *et al.*, Magnetic memory of a single-molecule quantum magnet wired to a gold surface, Nat. Mater. **8**, 194 (2009).

[2] D. Stepanenko, T. Mircea, and D. Loss, Quantum computing with molecular magnets, Inorg. Chim. Acta **361**, 3740 (2008).

[3] E. Moreno-Pineda, C. Godfrin, F. Balestro, W. Wernsdorfer, and M. Ruben, Molecular spin qudits for quantum algorithms, Chem. Soc. Rev. **47**, 501 (2018).

[4] M. Misiorny and J. Barnaś, Magnetic switching of a single molecular magnet due to spin-polarized current, Phys. Rev. B **75**, 134425 (2007).

[5] K. Hymas and A. Soncini, Molecular spintronics using single-molecule magnets under irradiation, Phys. Rev. B **99**, 245404 (2019).

[6] A. Candini, S. Klyatskaya, M. Ruben, W. Wernsdorfer, and M. Affronte, Graphene spintronic devices with molecular nanomagnets, Nano Lett. **11**, 2634 (2011).

[7] M. Urdampilleta, S. Klyatskaya, J.-P. Cleuziou, M. Ruben, and W. Wernsdorfer, Supramolecular spin valves, Nat. Mater. **10**, 502 (2011).

[8] M. Urdampilleta, S. Klayatskaya, M. Ruben, and W. Wernsdorfer, Magnetic interaction between a radical spin and a single-molecule magnet in a molecular spin-valve, ACS Nano **9**, 4458 (2015).

[9] L. Vitali, S. Fabris, A. M. Conte, S. Brink, M. Ruben, S. Baroni, and K. Kern, Electronic structure of surface-supported bis (phthalocyaninato) terbium (III) single molecular magnets, Nano Lett. **8**, 3364 (2008).

[10] J. Gómez-Segura, I. Díz-Pérez, N. Ishikawa, M. Nakano, J. Veciana, and D. Ruiz-Molina, 2-D Self-assembly of the bis (phthalocyaninato) terbium (III) single-molecule magnet studied by scanning tunneling microscopy, Chem. Commun. **27**, 2866 (2006).

[11] R. Vincent, S. Klyatskaya, M. Ruben, W. Wernsdorfer, and F. Balestro, Electronic read-out of a single nuclear spin using a molecular spin transistor, Nature (London) **488**, 357 (2012).

[12] S. Thiele, F. Balestro, R. Ballou, S. Klyatskaya, M. Ruben, and W. Wernsdorfer, Electrically driven nuclear spin resonance in single-molecule magnets, Science **344**, 1135 (2014).

[13] C. Godfrin, S. Lumetti, H. Biard, E. Bonet, S. Klyatskaya, M. Ruben, A. Candini, M. Affronte, W. Wernsdorfer, and F. Balestro, Microwave-assisted reversal of a single electron spin, J. Appl. Phys. **125**, 142801 (2019).

[14] S. Thiele, R. Vincent, M. Holzmann, S. Klyatskaya, M. Ruben, W. Wernsdorfer, and F. Balestro, Electrical Readout of Individual Nuclear Spin Trajectories in A Single-Molecule Magnet Spin Transistor, Phys. Rev. Lett. **111**, 037203 (2013).

[15] C. Godfrin, A. Ferhat, R. Ballou, S. Klyatskaya, M. Ruben, W. Wernsdorfer, and F. Balestro, Operating Quantum States in Single Magnetic Molecules: Implementation of Grover's Quantum Algorithm, Phys. Rev. Lett. **119**, 187702 (2017).

[16] M. Urdampilleta, S. Klyatskaya, M. Ruben, and W. Wernsdorfer, Landau-Zener tunneling of a single Tb^{3+} magnetic moment allowing the electronic read-out of a nuclear spin, Phys. Rev. B **87**, 195412 (2013).

[17] I. V. Krainov, J. Klier, A. P. Dmitriev, S. Klyatskaya, M. Ruben, W. Wernsdorfer, and I. V. Gornyi, Giant magnetoresistance

in carbon nanotubes with single-molecule magnets $TbPc_2$, ACS Nano **11**, 6868 (2017).

[18] F. Troiani, C. Godfrin, S. Thiele, F. Balestro, W. Wernsdorfer, S. Klyatskaya, M. Ruben, and M. Affronte, Landau-Zener Transition in A Continuously Measured Single-Molecule Spin Transistor, Phys. Rev. Lett. **118**, 257701 (2017).

[19] C. Godfrin, S. Thiele, A. Ferhat, S. Klyatskaya, M. Ruben, W. Wernsdorfer, and F. Balestro, Electrical read-out of a single spin using an exchange-coupled quantum dot, ACS Nano **11**, 3984 (2017).

[20] D. Komijani, A. Ghirri, C. Bonizzoni, S. Klyatskaya, E. Moreno-Pineda, M. Ruben, A. Soncini, M. Affronte, and S. Hill, Radical-lanthanide ferromagnetic interaction in a Tb^{III} bis-phthalocyaninato complex, Phys. Rev. Materials **2**, 024405 (2018).

[21] S. Marocchi, A. Candini, D. Klar, W. Van den Heuvel, H. Huang, F. Troiani, V. Corradini, R. Biagi, V. De Renzi, S. Klyatskaya *et al.*, Relay-like exchange mechanism through a spin radical between $TbPc_2$ molecules and graphene/Ni(111) substrates, ACS Nano **10**, 9353 (2016).

[22] R. Pederson, A. L. Wysocki, N. Mayhall, and K. Park, Multireference ab initio studies of magnetic properties of terbium-based single-molecule magnets, J. Phys. Chem. A **123**, 6996 (2019).

[23] H. Huang, W. Van den Heuvel, and A. Soncini, Lanthanide-radical magnetic coupling in $[LnPc_2]^0$: Competing exchange mechanisms captured via ab initio multi-reference calculations, Quantum Mater. Res. **1**, e200003 (2020).

[24] H. Heersche, Z. De Groot, J. Folk, H. Van Der Zant, C. Romeike, M. Wegewijs, L. Zobbi, D. Barreca, E. Ton-dello, and A. Cornia, Electron Transport through Single Mn_12 Molecular Magnets, Phys. Rev. Lett. **96**, 206801 (2006).

[25] E. Burzurí, A. S. Zyazin, A. Cornia, and H. S. J. Van der Zant, Direct Observation of Magnetic Anisotropy in An Individual Fe_4 Single-Molecule Magnet, Phys. Rev. Lett. **109**, 147203 (2012).

[26] N. Ishikawa, M. Sugita, T. Okubo, N. Tanaka, T. Iino, and Y. Kaizu, Determination of ligand-field parameters and f-electronic structures of double-decker bis (phthalocyaninato) lanthanide complexes, Inorg. Chem. **42**, 2440 (2003).

[27] A. Candini, D. Klar, S. Marocchi, V. Corradini, R. Bi-agi, V. De Renzi, U. del Pennino, F. Troiani, V. Bellini, S. Klyatskaya *et al.*, Spin-communication channels between Ln (III) bis-phthalocyanines molecular nanomagnets and a magnetic substrate, Sci. Rep. **6**, 21740 (2016).

[28] R. A. Jishi, *Feynman Diagram Techniques in Condensed Matter Physics* (Cambridge University Press, Cambridge, 2013).

[29] J. Iñarrea, G. Platero and A. H. MacDonald, Electronic transport through a double quantum dot in the spin-blockade regime: Theoretical models, Phys. Rev. B **76**, 085329 (2007).

[30] D. Averin and Y. V. Nazarov, Virtual Electron Diffusion during Quantum Tunneling of the Electric Charge, Phys. Rev. Lett. **65**, 2446 (1990).

[31] V. N. Golovach and D. Loss, Transport through a double quantum dot in the sequential tunneling and cotunneling regimes, Phys. Rev. B **69**, 245327 (2004).

[32] C. Timm and F. Elste, Spin amplification, reading, and writing in transport through anisotropic magnetic molecules, Phys. Rev. B **73**, 235304 (2006).

[33] R. Hanson, B. Witkamp, L. Vandersypen, L. W. van Beveren, J. Elzerman, and L. Kouwenhoven, Single-Shot Readout of Electron Spin States in A Quantum dot Using Spin-Dependent Tunnel Rates, Phys. Rev. Lett. **91**, 196802 (2003).

[34] E. V. Sukhorukov, G. Burkard, and D. Loss, Noise of a quantum dot system in the cotunneling regime, Phys. Rev. B **63**, 125315 (2001).

[35] H.-A. Engel and D. Loss, Single-spin dynamics and decoherence in a quantum dot via charge transport, Phys. Rev. B **65**, 195321 (2002).

[36] F. Elste and C. Timm, Cotunneling and nonequilibrium magnetization in magnetic molecular monolayers, Phys. Rev. B **75**, 195341 (2007).

[37] P. Recher, E. V. Sukhorukov, and D. Loss, Quantum dot as Spin Filter and Spin Memory, Phys. Rev. Lett. **85**, 1962 (2000).

[38] N. Ishikawa, M. Sugita, and W. Wernsdorfer, Quantum tunneling of magnetization in lanthanide single-molecule magnets: bis (phthalocyaninato) terbium and bis (phthalocyaninato) dysprosium anions, Angew. Chem. Int. **44**, 2931 (2005).